



An Infrared Census of DUST in Nearby Galaxies with *Spitzer* (DUSTiNGS). IV. Discovery of High-redshift AGB Analogs*

M. L. Boyer¹, K. B. W. McQuinn², M. A. T. Groenewegen³, A. A. Zijlstra^{4,5}, P. A. Whitelock^{6,7}, J. Th. van Loon⁸,
G. Sonneborn⁹, G. C. Sloan^{1,10}, E. D. Skillman¹¹, M. Meixner¹, I. McDonald⁴, O. C. Jones¹, A. Javadi¹², R. D. Gehrz¹¹,
N. Britavskiy¹³, and A. Z. Bonanos¹⁴

¹ STScI, 3700 San Martin Drive, Baltimore, MD 21218, USA; mboyer@stsci.edu

² University of Texas at Austin, McDonald Observatory, 2515 Speedway, Stop C1402, Austin, TX 78712, USA

³ Royal Observatory of Belgium, Ringlaan 3, B-1180 Brussels, Belgium

⁴ Jodrell Bank Centre for Astrophysics, Alan Turing Building, University of Manchester, M13 9PL, UK

⁵ Department of Physics & Laboratory for Space Research, University of Hong Kong, Pokfulam Road, Hong Kong

⁶ Astronomy Department, University of Cape Town, 7701 Rondebosch, South Africa

⁷ South African Astronomical Observatory (SAAO), P.O. Box 9, 7935 Observatory, South Africa

⁸ Lennard-Jones Laboratories, Keele University, ST5 5BG, UK

⁹ Observational Cosmology Lab, Code 665, NASA Goddard Space Flight Center, Greenbelt, MD 20771, USA

¹⁰ Department of Physics and Astronomy, University of North Carolina, Chapel Hill, NC 27599-3255, USA

¹¹ Minnesota Institute for Astrophysics, School of Physics and Astronomy, 116 Church Street SE, University of Minnesota, Minneapolis, MN 55455 USA

¹² School of Astronomy, Institute for Research in Fundamental Sciences (IPM), P.O. Box 19395-5531, Tehran, Iran

¹³ Instituto de Astrofísica de Canarias, E-38205 La Laguna 38200, Tenerife, Spain

¹⁴ IAASARS, National Observatory of Athens, GR-15236 Penteli, Greece

Received 2017 September 18; revised 2017 October 27; accepted 2017 November 4; published 2017 December 22

Abstract

The survey for DUST in Nearby Galaxies with *Spitzer* (DUSTiNGS) identified several candidate Asymptotic Giant Branch (AGB) stars in nearby dwarf galaxies and showed that dust can form even in very metal-poor systems ($Z \sim 0.008 Z_{\odot}$). Here, we present a follow-up survey with WFC3/IR on the *Hubble Space Telescope* (HST), using filters that are capable of distinguishing carbon-rich (C-type) stars from oxygen-rich (M-type) stars: F127M, F139M, and F153M. We include six star-forming DUSTiNGS galaxies (NGC 147, IC 10, Pegasus dIrr, Sextans B, Sextans A, and Sag DIG), all more metal-poor than the Magellanic Clouds and spanning 1 dex in metallicity. We double the number of dusty AGB stars known in these galaxies and find that most are carbon rich. We also find 26 dusty M-type stars, mostly in IC 10. Given the large dust excess and tight spatial distribution of these M-type stars, they are most likely on the upper end of the AGB mass range (stars undergoing Hot Bottom Burning). Theoretical models do not predict significant dust production in metal-poor M-type stars, but we see evidence for dust excess around M-type stars even in the most metal-poor galaxies in our sample ($12 + \log(\text{O}/\text{H}) = 7.26\text{--}7.50$). The low metallicities and inferred high stellar masses (up to $\sim 10 M_{\odot}$) suggest that AGB stars can produce dust very early in the evolution of galaxies (~ 30 Myr after they form), and may contribute significantly to the dust reservoirs seen in high-redshift galaxies.

Key words: galaxies: dwarf – stars: AGB and post-AGB – stars: carbon – stars: mass-loss – techniques: photometric

Supporting material: machine-readable table

1. Introduction

The shape of the initial mass function establishes low- and intermediate-mass stars ($\sim 0.8\text{--}10 M_{\odot}$) as a dominant contributor to the stellar populations of galaxies. These stars pass through the thermally pulsing Asymptotic Giant Branch (TP-AGB)¹⁵ phase at the end of their evolution, during which time the products of nucleosynthesis are returned to the interstellar medium (ISM) via a strong stellar wind that ultimately ends the evolution of the star. The rich diversity of elements and the dust produced during this phase make AGB stars a key driver of galactic evolution.

Dust in high-redshift galaxies is often attributed to AGB stars and supernovae (e.g., Valiante et al. 2009; Dwek &

Cherchneff 2011; Rowlands et al. 2014; Michałowski 2015), though the relative contributions from each is not well understood. For supernovae, the uncertainty lies in the balance between dust creation and destruction. For AGB stars, the chief uncertainty lies in the metallicity dependence of dust production. Some studies show a clear metallicity effect in carbon-rich AGB stars (van Loon et al. 2008), while others suggest that C star dust production has weak-to-no metallicity dependence (Sloan et al. 2012, 2016; Boyer et al. 2015c). It is, however, the dusty M-type AGB stars that may be more important at early times because the most massive AGB stars (and thus those that can produce dust on the shortest timescales) are O-rich. While dredge-up of newly formed carbon converts AGB stars into C stars, a process called hot bottom burning (HBB) occurs when the base of the convective envelope dips into the H-shell, resulting in nuclear burning of ^{12}C into ^{14}N and thus limiting the formation of C stars (Boothroyd et al. 1993). This occurs only in AGB stars more massive than ~ 3 or $4 M_{\odot}$, depending

* Based on observations made with the NASA/ESA Hubble Space Telescope at the Space Telescope Science Institute, which is operated by the Association of Universities for Research in Astronomy, Inc., under NASA contract NAS 5-26555. These observations are associated with program GO-14073.

¹⁵ Unless otherwise noted, we use the term AGB to denote TP-AGB stars throughout this paper.

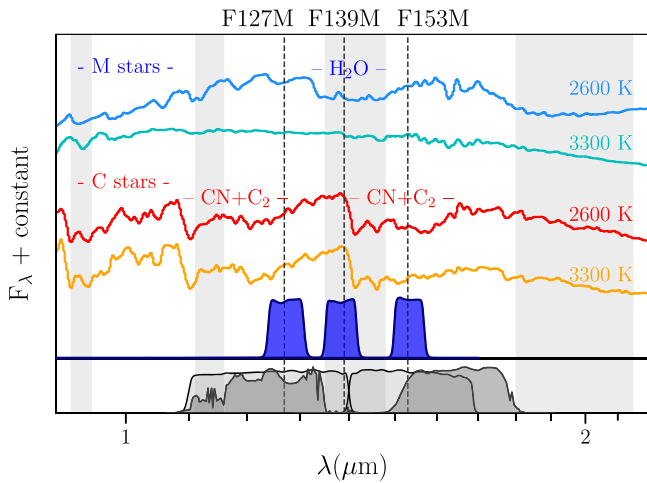


Figure 1. WFC3/IR medium-band filters (blue) used here to distinguish C-type (red) and M-type (blue) stars by sampling the water feature in M-type stars and the CN+C₂ feature in C-type stars near 1.4 μm . The model spectra are from Aringer et al. (2009, 2016). In the lower panel, we show the 2MASS *J* and *H* filters (dark gray) and WFC3/IR F125W and F160W filters (light gray) for reference (transmissions not to scale).

on the metallicity (Ventura et al. 2012; Karakas & Lugaro 2016; Marigo et al. 2017). As a result, M-type AGB stars could inject dust into the ISM as early as 30 Myr after forming (for a 10 M_{\odot} star). Dusty C stars, on the other hand, contribute much later ($t_{\text{lifetime}} \approx 0.3\text{--}3.6$ Gyr).

Unlike C stars, M-type stars do not produce their own condensable material (typically silicon, iron, magnesium, and oxygen), so the efficiency of dust production is expected to strongly decrease with metallicity. This expected metallicity dependence has, however, been difficult to quantify observationally both due to the comparative rarity of dust-producing M-type stars and to the limited range of metallicities reachable with IR observatories. AGB dust production in the Magellanic Clouds ($Z/Z_{\odot} \approx 0.2$ and 0.5) has been extensively studied (e.g., van Loon et al. 1998, 2008; Trams et al. 1999; van Loon 2006; Groenewegen et al. 2007, 2009; Riebel et al. 2012; Srinivasan et al. 2016; Goldman et al. 2017), but there are few examples of dust-producing AGB stars at lower metallicities.

A handful of dusty stars have been confirmed in dwarf spheroidal (dSph) galaxies with metallicities as low as $[\text{Fe}/\text{H}] \sim -1$. (Lagadec et al. 2007; Matsuura et al. 2007; Sloan et al. 2009, 2012; Whitelock et al. 2009; Menzies et al. 2010, 2011; McDonald et al. 2014) and in globular clusters with $[\text{Fe}/\text{H}] > -1.6$ (Boyer et al. 2008, 2009; McDonald et al. 2009, 2011). All of these examples are C stars or low-mass M-type stars. The globular cluster stars (low-mass M-type; $\approx 0.8\text{--}1.5 M_{\odot}$) do appear to produce dust despite their low metallicities. However, these may not be true analogs of more massive O-rich AGB dust producers at early epochs because (1) low-mass stars generally produce only modest amounts of dust, (2) most are observed in globular clusters where pollution from earlier populations is a widespread phenomenon (Gratton et al. 2004, 2012; Prantzos et al. 2007), and (3) the mixing and nucleosynthesis processes that occur in low-mass and high-mass O-rich AGB stars are fundamentally different (Karakas & Lattanzio 2014).

To search for examples of high-mass AGB dust production, environments with large stellar populations and recent star formation must be studied. Several dwarf galaxies in and around the Local Group are suitable, but their large distances

make IR observations difficult. A few studies (Jackson et al. 2007a, 2007b; Boyer et al. 2009; Davidge 2014; Jones et al. 2014) have statistically inferred the presence of dust-producing AGB stars in several star-forming dwarf galaxies, but were unable to identify individual dusty stars due both to confusion with unresolved background galaxies and to substantial circumstellar extinction at optical wavelengths. At these distances, additional information is necessary to confidently identify individual dusty AGB stars. McQuinn et al. (2007) and Javadi et al. (2013) exploited stellar variability to identify dust-producing AGB stars in M33 and the survey of DUST in Nearby Galaxies with *Spitzer* (DUSTiNGS; Boyer et al. 2015b, Paper I) used a similar strategy to identify dusty AGB variables in very metal-poor galaxies. DUSTiNGS observed 50 nearby galaxies and identified 526 dusty AGB candidates by their IR excesses and brightness changes between 2 epochs, with particular sensitivity to stars with 300–600 day periods. Assuming all candidates are indeed producing dust, Boyer et al. (2015c, Paper II) found that AGB dust forms even at metallicities as low as $0.006 Z_{\odot}$. The lack of a correlation between dust production and metallicity in the DUSTiNGS galaxies suggests that AGB stars can be a dominant source of dust even in metal-deficient early galaxies. However, Paper II was unable to confirm the AGB nature of these sources or identify the AGB spectral type (and hence whether the dust comprises silicate or carbon grains).

In this paper, we present near-IR *Hubble Space Telescope* (*HST*) observations of six star-forming DUSTiNGS galaxies. Combined with mid-IR *Spitzer* data, the *HST* data reveal whether the atmospheric chemistry of the dust-producing stars is carbon- or oxygen-rich. In addition to the confirmation of 120 dusty carbon stars, we confirm 26 dust-producing M-type stars in this sample, showing that *massive* AGB stars can contribute dust at extremely low metallicity. In Section 2, we describe the survey and stellar classifications. In Section 3, we discuss the properties of the dustiest stars.

2. Data and Analysis

2.1. Identifying AGB Spectral Types with *HST*

Photometric surveys typically separate C- and M-type stars using broadband near-IR or narrow-band optical filters. The broadband near-IR filters (*JHK*) are influenced by VO, TiO, and H₂O molecular features in M-type stars and CN and C₂ in C stars, while the narrow-band filters target TiO and CN molecular features at $\lambda < 7000$ Å. The optical surveys are severely photon-limited and fail to detect the stars with even moderate circumstellar dust extinction. The near-IR *JHK* surveys capture more of the dusty stars, but classification is imprecise (Boyer et al. 2013, 2015a; Ruffle et al. 2015; Jones et al. 2017) and the dustiest stars, which can be faint even in the near-IR, generally remain undetected because of source confusion and insufficient sensitivity from the ground, especially in the *K* band. These impediments are overcome here with the IR channel of *HST*'s Wide-Field Camera 3 (WFC3; Kimble et al. 2008), which has ample sensitivity and angular resolution in the near-IR for detecting AGB stars out to the edge of the Local Group.

Most *HST* surveys use the wide WFC3 filters (especially F110W and F160W; Dalcanton et al. 2012a, 2012b; Sabbi et al. 2013) to maximize the imaging depth, but these filters are too wide to be influenced by molecular absorption features in

Table 1
Target Information

Galaxy	Alt. Name	Morph. Type (Mpc)	d	[Fe/H]	$12 + \log(\text{O}/\text{H})$ (mag)	M_V (mag)	A_V
NGC 147	DDO 3	dE/dSph	0.76	-1.11	...	-14.6 ± 0.1	0.47
IC 10	UGC 192	dIrr	0.77	-1.28	8.19 ± 0.15	-15.0 ± 0.2	2.33
Pegasus	DDO 216	dTrans/dIrr	0.98	-1.4 ± 0.20	7.93 ± 0.13	-12.2 ± 0.2	0.19
Sextans B	DDO 70	dIrr	1.43	-1.6 ± 0.10	7.53 ± 0.05	-14.5 ± 0.2	0.09
Sextans A	DDO 75	dIrr	1.46	-1.85	7.54 ± 0.06	-14.3 ± 0.1	0.12
Sag DIG	Sgr dIG	dIrr	1.09	-2.1 ± 0.20	7.26–7.50	-11.5 ± 0.3	0.34

Note. Distances are derived from F814W (I -band) TRGB estimates from McQuinn et al. (2017, Paper III). A_V is from Weisz et al. (2014). M_V is from McConnachie (2012) and references therein. The values of [Fe/H] adopted here are derived from RGB colors from Nowotny et al. (2003), Bellazzini et al. (2014), Tikhonov & Galazutdinova (2009), McConnachie et al. (2005), Momany et al. (2002), and Sakai et al. (1996). Stellar metallicities are derived from spectroscopy of RGB stars in NGC 147 agree with our adopted value (Geha et al. 2010). However, Kirby et al. (2017) measured [Fe/H] = $-1.88^{+0.13}_{-0.09}$ from RGB star spectroscopy in Sag DIG. ISM gas-phase oxygen abundances ($12 + \log(\text{O}/\text{H})$) are from from Mateo (1998), Lee et al. (2006), and Saviane et al. (2002).

AGB star spectra, resulting in significant color overlap between these spectral types. Boyer et al. (2013) demonstrated the use of *HST* WFC3/IR medium-band filters to successfully separate C- and M-type stars in a field in the inner disk of M31. These filters fall within the H_2O and $\text{CN}+\text{C}_2$ features at 1.2–1.5 μm (filters: F127M, F139M, and F153M, Figure 1), thus firmly dividing the two spectral types with minimal cross-contamination. Furthermore, even the dustiest stars remain separated by spectral type in the WFC3/IR colors, unlike in $J-K$ colors which overlap significantly once dust is included.

2.2. Sample Selection

We observed six DUSTiNGS galaxies with *HST*'s WFC3/IR in Cycle 23 as part of GO-14073 from 2016 October to 2016 August. Table 1 lists the observed galaxies and their properties. We chose these six galaxies because they have large populations of dust-producing AGB candidates and span the entire metallicity range of the DUSTiNGS sample. Four of the galaxies are gas-rich dwarf irregular (dIrr) systems with H II regions that point to sites of current massive star formation. One galaxy (Pegasus/DDO 216) is a transition-type galaxy (dTrans). It is gas-rich, but there are no H II regions. One galaxy (NGC 147) is a dwarf spheroidal (dSph). It is a gas-poor galaxy with no current star formation, but a sizeable intermediate-aged AGB population is evident (e.g., Lorenz et al. 2011; Hamedani Golshan et al. 2017). The star formation histories of all six galaxies are described by Weisz et al. (2014).

The $2'1 \times 2'3$ WFC3/IR field of view is very small compared to the DUSTiNGS footprint ($\gtrsim 10' \times 10'$), so we observed galaxies with two or three fields, placed to maximize the coverage of DUSTiNGS AGB candidates while also maximizing the inclusion of those with $[3.6]-[4.5] > 0.5$ mag, i.e., the dustiest stars. Figure 2 shows the placement of the WFC3/IR fields. In total, we have covered 99 of the 375 original DUSTiNGS x-AGB variables reported for these six galaxies in Paper II.

2.3. Observations and Photometry

Observations are summarized in Table 2. We imaged each field with the F127M, F139M, and F153M filters, employing four dithers with the WFC3-IR-DITHER-BOX-MIN pattern to minimize image defects and to maximize the spatial resolution (the resulting mosaics are Nyquist sampled). The total exposure times are 796.9–896.9 s in each filter, depending on the detector sampling sequence used. WFC3/IR is

non-destructively read out multiple times during an exposure using sequences combining long and short reads that provide uniform sampling over a wide range of stellar magnitudes (MULTIACCUM mode¹⁶). For the first three exposures in each filter, we adopted sample sequence STEP100 with NSAMP = 8. The fourth and final exposure for each filter was set to fit within the remaining orbit visibility, which differed for each galaxy: STEP100, NSAMP = 8; STEP100, NSAMP = 9; STEP50, NSAMP = 10; or SPARS25, NSAMP = 12.

We used *HST* Drizzlepac v2.0 to create mosaics in each filter. We combined the calibrated, flat-fielded exposures (flt.fits files) using ASTRODRIZZLE to create a stacked, drizzled image with pixel scale 0''.0642/pix. Stellar positions were measured on the drizzled F127M image, allowing for forced photometry of faint stars in the individual images.

We performed PSF photometry on the flt.fits images using DOLPHOT's WFC3-specific module (Dolphin 2000). We retain only stars with error flag <8 and signal-to-noise >4 and require low sharpness and crowding values. Restricting the sharpness parameter minimizes contamination from extended sources and cosmic rays, and restricting the crowding parameter ensures that a star's flux measurement is not substantially affected by nearby stars. We adopt $(\Sigma \text{Sharp}_\lambda)^2 < 0.1$ and $(\Sigma \text{Crowd}_\lambda) < 1.5$ mag. The crowd parameter is a measure of how much brighter a star would be if nearby stars were not subtracted simultaneously. The sharp parameter is positive for sharp sources (cosmic rays) and negative for extended sources. These initial quality cuts eliminate most contamination and poor measurements from the catalog, but inspection of the images suggests that some extended and/or blended sources remain. We therefore flag sources with $(\Sigma \text{Sharp}_\lambda)^2 > 0.02$ as those that require further scrutiny.

Artificial star tests indicate that photometry is >90% complete at S/N > 10. Since our AGB analysis is restricted to sources brighter than this limit, our AGB samples are near-complete. To identify dust-producing stars, we use *Spitzer* photometry from Paper I. We use the magnitudes measured after coadding the two observing epochs to mitigate the effect of pulsation in the IR data.

The *HST* catalog was matched to the *Spitzer* catalog using the DAOMaster routine (Stetson 1987), which iteratively solves for the transformation coefficients and assigns matches,

¹⁶ http://www.stsci.edu/hst/wfc3/documents/handbooks/currentIHB/c07_ir08.html

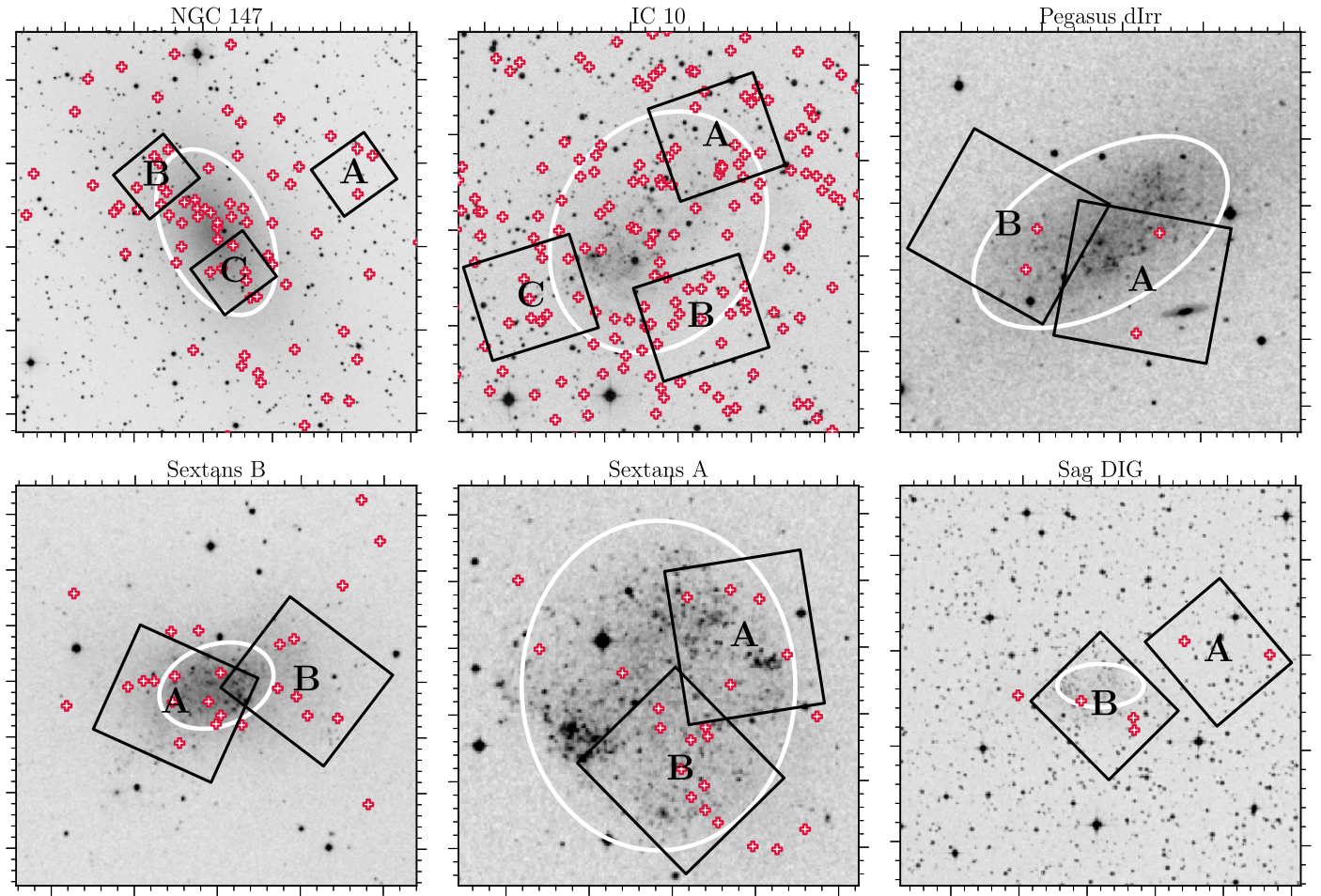


Figure 2. DSS images of the six target galaxies with north pointing up and east to the left. Black boxes mark the *HST* footprints ($123'' \times 136''$), labeled A, B, and C (Table 2). White ellipses mark the half-light radii of the galaxies. The dusty AGB variables from DUSTiNGS are marked with red plus symbols (Boyer et al. 2015c). Fields were selected to maximize the number of DUSTiNGS variables covered and to include the dustiest examples.

Table 2
Observations

Galaxy	Field	R.A. (J2000)	Decl. (J2000)	Start Date (UT)	F127M t_{exp} (s)	F139M t_{exp} (s)	F153M t_{exp} (s)	Orient. (E of N)
IC 10	A	00 ^h 20 ^m 08 ^s .22	+59 ^d 20 ^m 25 ^s .68	2015 Oct 18 04:56:34	875.6	896.9	896.9	22 ^o 9
IC 10	B	00 ^h 20 ^m 08 ^s .83	+59 ^d 16 ^m 37 ^s .24	2015 Oct 19 04:48:44	875.6	896.9	896.9	21 ^o 6
IC 10	C	00 ^h 20 ^m 36 ^s .95	+59 ^d 16 ^m 48 ^s .82	2015 Oct 19 16:38:31	875.6	896.9	896.9	21 ^o 1
NGC 147	A	00 ^h 32 ^m 41 ^s .89	+48 ^d 32 ^m 44 ^s .21	2015 Oct 09 22:28:15	846.9	875.6	846.9	35 ^o 2
NGC 147	B	00 ^h 33 ^m 24 ^s .92	+48 ^d 32 ^m 40 ^s .26	2015 Oct 07 02:57:33	846.9	875.6	846.9	39 ^o 5
NGC 147	C	00 ^h 33 ^m 08 ^s .14	+48 ^d 29 ^m 12 ^s .66	2015 Oct 09 02:59:39	846.9	875.6	846.9	36 ^o 5
Pegasus dIrr	A	23 ^h 28 ^m 33 ^s .15	+14 ^d 43 ^m 54 ^s .62	2015 Oct 02 06:57:09	796.9	825.6	796.9	-10 ^o 1
Pegasus dIrr	B	23 ^h 28 ^m 41 ^s .42	+14 ^d 44 ^m 41 ^s .16	2015 Oct 04 07:07:30	796.9	825.6	796.9	-28 ^o 9
Sag DIG	A	19 ^h 29 ^m 48 ^s .07	-17 ^d 39 ^m 59 ^s .21	2016 Aug 07 13:47:10	796.9	846.9	796.9	-49 ^o 0
Sag DIG	B	19 ^h 29 ^m 58 ^s .04	-17 ^d 41 ^m 07 ^s .73	2016 Aug 07 14:46:50	796.9	846.9	796.9	-44 ^o 6
Sextans A	A	10 ^h 10 ^m 55 ^s .20	-04 ^d 40 ^m 56 ^s .64	2016 Mar 06 04:03:59	796.9	825.6	796.9	-81 ^o 1
Sextans A	B	10 ^h 10 ^m 58 ^s .91	-04 ^d 42 ^m 51 ^s .65	2016 Apr 04 01:21:55	796.9	825.6	796.9	-45 ^o 8
Sextans B	A	10 ^h 00 ^m 02 ^s .49	+05 ^d 19 ^m 38 ^s .36	2016 Mar 14 02:54:20	796.9	825.6	796.9	-24 ^o 1
Sextans B	B	09 ^h 59 ^m 53 ^s .00	+05 ^d 20 ^m 00 ^s .84	2016 Mar 17 17:08:40	796.9	825.6	796.9	-37 ^o 2

Note. This data is from *HST* program GO-14073 (P.I. Boyer; doi:10.17909/T9HM3M).

starting with a $3''$ radius and decreasing to a $0''.6$ radius. The *HST* and *Spitzer* data are poorly matched in both spatial resolution and sensitivity; to minimize mismatches between these two data sets, we restrict the *HST* input catalog to stars with signal-to-noise (S/N) >10 in all three filters thereby

excluding the faintest stars that are unlikely to have *Spitzer* counterparts. IC 10 is the most densely populated galaxy in our sample, and the lower-resolution *Spitzer* data are therefore strongly affected by crowding (Paper I). We thus restrict the IC 10 *HST* catalog to S/N >15 to achieve a good match to

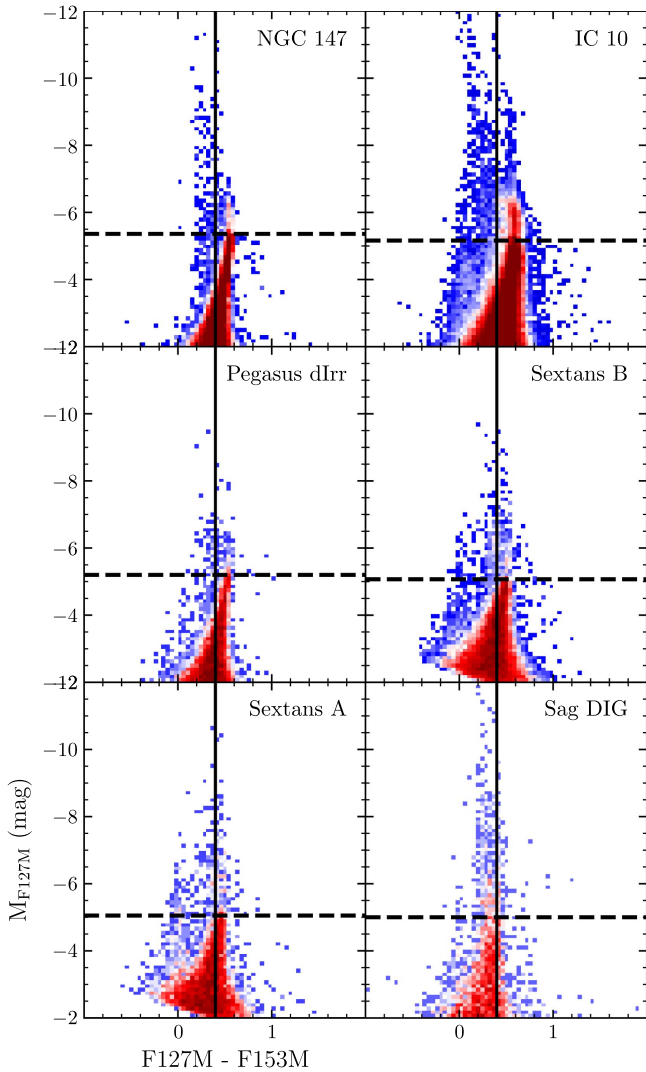


Figure 3. *HST* color–magnitude diagrams including stars with $S/N > 4$ (red: higher source density, blue: lower source density). The dashed red line marks the TRGB (Section 2.4.1). The solid line at $F_{127M} - F_{153M} = 0.4$ mag is for reference. The main sequence is visible in most panels at a color of 0 mag. Foreground stars are in the vertical sequence just to the left of the solid line and are especially prominent in IC 10 and Sag DIG, which are near the Galactic Plane.

the *Spitzer* sources. We manually checked all DUSTiNGS x-AGB variables from Paper II that were not matched to *HST* sources using these criteria. Six DUSTiNGS variables match *HST* sources with low S/N , and these were added back into the catalogs.

All photometry presented in this paper is corrected for extinction using the A_V values listed by Weisz et al. (2014). That work takes values from Schlafly & Finkbeiner (2011) if $A_V < 0.2$. Higher extinction values were estimated by comparing observed and simulated optical color–magnitude diagrams. We assume $A_{F_{127M}}/A_V = 0.27391$, $A_{F_{139M}}/A_V = 0.23979$, $A_{F_{153M}}/A_V = 0.20366$, $A_{3.6}/A_V = 0.06706$, and $A_{4.5}/A_V = 0.05591$, from the Padova simulations.¹⁷

Figure 3 shows the *HST* color–magnitude diagrams, and Table 3 lists the columns included in the final catalog, available to download in the electronic version of this paper and on VizieR. We have made no corrections to the *HST* astrometry,

Table 3
Catalog Information

Column Number	Column Description
1	Identification number
2	DUSTiNGS ID
3	Galaxy name
4	R.A. (J2000)
5	Decl. (J2000)
6–7	F_{127M} magnitude and 1σ error
8–9	F_{139M} magnitude and 1σ error
10–11	F_{153M} magnitude and 1σ error
12–13	[3.6] magnitude and 1σ error ^a
14–15	[4.5] magnitude and 1σ error ^a
16	C or M classification
17	x-AGB variable Flag ^b
18	Dusty flag ^c
19	Contamination flag ^d

Notes. The catalog is available with the electronic version of this paper and on VizieR.

^a Magnitudes are from the coadded epochs (≈ 180 days separation). See Paper I.

^b The x-AGB variables identified in Paper II.

^c Sources with $>4\sigma$ excess in [3.6]–[4.5].

^d Sources that are suspected contaminants (Section 2.5).

(This table is available in its entirety in machine-readable form.)

which has ≈ 200 mas absolute accuracy and ≈ 10 mas relative accuracy.¹⁸ The *Spitzer* positions are aligned to 2MASS by the *Spitzer* pipeline and thus have an absolute astrometric accuracy ≈ 150 mas.

2.4. Classification

To select C- and M-type stars, we first measure the tip of the red giant branch (TRGB). Once sub-TRGB stars are eliminated, we use the Aringer et al. (2009, 2016) models to define color cuts that separate AGB spectral types. In all six galaxies, we find a total of 908 C stars and 2120 M stars; Table 4 lists the final adopted star counts.

2.4.1. TRGB

To find the TRGB in each filter, we follow the commonly used strategy described by Méndez et al. (2002). First, we select stars with $F_{129M} - F_{153M} > 0.1$ mag to eliminate main-sequence stars. Next, we pass the Gaussian-smoothed luminosity function through a Sobel edge-detection filter. We perform 500 Monte Carlo Bootstrap resampling trials, each time adding 4σ Gaussian random photometric errors and random variations on the bin size and starting magnitude of the luminosity function. The final TRGB and its uncertainty are the mean and standard deviation of a Gaussian function fit to the TRGB estimates from the 500 trials (Table 5). Other techniques to find the TRGB can result in more precise measurements than the edge-detector method we employ, such as Bayesian maximum likelihood (e.g., Makarov et al. 2006; Conn et al. 2012; McQuinn et al. 2016). However, since our red giant branches are deep and well populated, Bayesian

¹⁷ <http://stev.oapd.inaf.it/cgi-bin/cmd>

¹⁸ http://www.stsci.edu/hst/wfc3/documents/handbooks/currentDHB/wfc3_dhb.pdf

Table 4
Source Counts

Galaxy	N_{TRGB}	C				M			
		All	Dusty ^a	Paper II ^b	Cont. ^c	All	Dusty ^a	Paper II ^b	Cont. ^c
IC 10	2928	531	49	26	5	1766	15	6	2
NGC 147	370	65	21	14	1	265	2	1	3
Pegasus	154	44	8	4	1	32	0	0	3
Sag DIG	149	16	4	3	6	3	2	0	3
Sextans A	386	65	14	10	3	9	3	1	0
Sextans B	545	187	24	11	5	45	4	1	0

Notes. N_{TRGB} indicates the number of stars brighter than the TRGB in F153M. C- and M-type stars are identified by their *HST* near-IR colors (Section 2.4.2).

^a The subset of C and M stars with $[3.6]-[4.5]$ color $>4\sigma$ that are not classified as contaminants. (Section 2.4.3).

^b The subset of C and M stars identified as x-AGB variables in Paper II not classified as contaminants.

^c The subset of C and M stars that show $>4\sigma$ dust excess, but are suspected contaminants based on their location in Figure 8.

Table 5
Near-IR TRGB

Galaxy	TRGB				
	F814W (mag)	F127M (mag)	F139M (mag)	F153M (mag)	$(m - M)_0$ (mag)
N 147	24.39 ± 0.06	19.03 ± 0.04	18.82 ± 0.04	18.45 ± 0.04	24.39 ± 0.06
IC 10	24.43 ± 0.03	19.27 ± 0.04	19.06 ± 0.04	18.68 ± 0.04	24.43 ± 0.03
Peg	24.96 ± 0.04	19.76 ± 0.05	19.55 ± 0.05	19.20 ± 0.05	24.96 ± 0.04
Sex B	25.77 ± 0.03	20.71 ± 0.05	20.52 ± 0.04	20.23 ± 0.05	25.77 ± 0.03
Sex A	25.82 ± 0.03	20.77 ± 0.09	20.58 ± 0.09	20.32 ± 0.09	25.82 ± 0.03
Sag	25.18 ± 0.04	20.18 ± 0.06	20.03 ± 0.06	19.77 ± 0.07	25.18 ± 0.04

Note. Distance moduli are derived from the F814W TRGB (Paper III), using the relationship from Rizzi et al. (2007). These are within 1σ of distance moduli listed by McConnachie (2012), except Pegasus dIrr (2σ) and NGC 147 (3σ).

techniques result in only a marginal gain in accuracy and reliability.

The TRGBs are fairly stable against metallicity in these filters, similar to the F814W TRGB (e.g., Rizzi et al. 2007). Using the distance moduli listed in Table 5, all three filters show brighter TRGBs at higher metallicity, with the F153M filter showing the largest metallicity effect ($\Delta\text{TRGB}(F127M/F139M/F153M) = 0.35/0.42/0.53$ mag).

2.4.2. Color–Color Selection

To select C- and M-type stars, we start with all sources brighter than the F153M TRGB. This restriction results in the loss of the dustiest AGB stars, which are made faint in F153M by circumstellar extinction. We recover these stars in Section 2.4.3.

Next, we classify the resulting subset of stars based on their location in the F127M–F139M versus F139M–F153M color–color diagram (CCD; Figure 4). When sub-TRGB stars are excluded (as they are here), this diagram has three main branches: an M-type branch, a C star branch, and a branch that includes a mixture of K-type stars, main-sequence stars, and foreground stars. We place the divisions in Figure 4 following the C, M, and K star models from Aringer et al. (2009, 2016). The C star models included in Figure 4 (plus symbols) are those with $-0.8 \leq \log g [\text{cm s}^{-2}] \leq 0$ and $\text{C}/\text{O} = 1.4$ (light orange), 2 (orange), and 5 (red). For the M/K stars (crosses), we include $T_{\text{eff}} \leq 3700$ K and $-1 \leq \log g [\text{cm s}^{-2}] \leq -0.5$; darker blue colors represent lower effective temperatures. Only models with $[\text{Fe}/\text{H}] \leq -1$ are included. The solid lines mark the adopted C- and M-type color divisions. Red and blue arrows illustrate the direction and magnitude of circumstellar extinction for $E(J - K_s) = 1$ mag for M-type stars with 60%

silicate + 40% AlOx and C stars with 70% amorphous carbon +30% SiC (Groenewegen 2006).

Both the C- and M-type models are slightly bluer than the data in both colors. This discrepancy (approximately 0.05 mag) has no effect on the C star definition since C stars are fairly well isolated from both M- and K-type stars. However, the discrepancy is large enough to substantially affect the number of M-type stars selected because of strong contamination from warmer K-type stars. The reason for the slight shifts between the models and data is unclear—one possibility is a bias in our adopted A_V values (Table 1). Another culprit might be the adopted water opacity in the models from Aringer et al. (2016), who note that other opacities shift the near-IR colors by about 0.05 mag. Furthermore, deviations from hydrostatic, spherically symmetric atmospheres and non-LTE conditions can affect the water opacity. Because of this slight color mismatch between the data and the models, we cannot use the exact colors of the models to define the transition from K-type stars to M-type stars (at around 3600 K) in the data. Instead, we note that M0+ models occupy the M/K-star sequence beginning just blueward of the knee in the CCD at F127M–F139M ≈ 0.2 mag and F139M–F153M ≈ 0.4 mag. We therefore select M-type stars based on the location of this knee in the data (Figure 5).

The adopted (F127M–F139M, F139M–F153M) positions of the C and M divisions in the CCD are as follows:

$$\text{M stars: } [(-0.6, 0.35), (0.35, 0.35), (1.0, 1.1)] \quad (1)$$

$$\text{C stars: } [(0.35, -0.75), (0.25, 0.00), (0.25, 0.23), (1.0, 1.1)]. \quad (2)$$

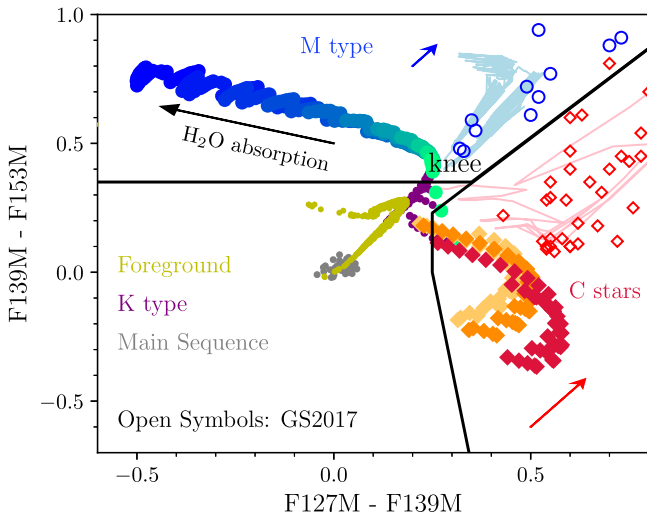


Figure 4. *HST* color-color diagram (CCD) showing the colors of C star models (orange/red filled diamonds; Aringer et al. 2009) and M/K star models (purple/cyan/blue filled circles; Aringer et al. 2016). Only models brighter than the TRGB (horizontal line in Figure 8) are plotted. Also shown in yellow are simulated foreground star colors (Girardi et al. 2005) and a representative sample of main-sequence stars in IC 10 (gray; $F127M - F153M < 0.1$ mag). K stars are marked in dark purple. The black lines mark the adopted C- and M-type regions. Red and blue arrows show the direction and magnitude of circumstellar extinction for C- and M-type stars, respectively (see the text). The open circles/diamonds are dusty M/C stars in the LMC from Groenewegen & Sloan (2017) and the light blue/pink lines show O-rich/C-rich COLIBRI models with Nanni et al. (2016) dust growth models ($\log \epsilon_s = -13$).

The line between C- and M-type stars on the right side of the CCD follows the direction of circumstellar extinction. Groenewegen & Sloan (2017; GS2017) fit ~ 500 dusty Magellanic Cloud stars using a modified version of the DUSTY radiative transfer code (Groenewegen 2012), and we passed the resulting spectral energy distributions (SEDs) through the medium-band *HST* filters used here. GS2017 used high-quality, multi-epoch data in the near-IR, so the SEDs used to derive the magnitudes in Figure 4 are well constrained around $1 \mu\text{m}$. The C- or M-type classification in GS2017 is based on features in the stars’ mid-IR spectra (e.g., Jones et al. 2017). We include the dustiest LMC stars from the GS2017 sample in Figure 4, with C-type stars as red open diamonds and M-type stars as blue open circles. With the exception of one star in Figure 4, the dusty C- and M-type stars stay separated on the *HST* CCD, indicating that contamination across the dividing line is low. For reference, we also show the COLIBRI tracks (Marigo et al. 2017), with Nanni et al. (2016) dust growth models.

We note that the GS2017 stars represent the dustiest examples of AGB stars. Less dusty examples that have not completely veiled their molecular features can fall along the entire H_2O and C/O sequences, with dust affecting the color as indicated by the blue and red extinction arrows in Figure 4.

2.4.3. Dusty Stars

Dusty AGB stars can be fainter than the TRGB both due to variability and to circumstellar extinction. To recover these sources, we turn to the *Spitzer* data. For both O-rich and C-rich stars in the Magellanic Clouds, the $[3.6] - [4.5]$ color is approximately proportional to the dust-production rates (Riebel

et al. 2012; Srinivasan et al. 2016; Sloan et al. 2016), especially at color > 0.1 mag (Figure 6). We therefore use the $[3.6] - [4.5]$ color as a proxy for dust excess, which we measure by comparing a source’s color to the mean color of stars within 1 mag bins at $4.5 \mu\text{m}$. We flag sources as dusty if the excess exceeds 4σ . Dusty objects that are fainter than the $F153M$ TRGB are included in our sample if they are brighter than the $3.6 \mu\text{m}$ TRGB (Paper III). There are examples of dusty carbon stars that are fainter than the $3.6 \mu\text{m}$ TRGB (e.g., in the LMC; Gruendl et al. 2008), but given the small stellar masses of our galaxies relative to the LMC, we expect to miss only a few such stars, if any, which does not impact our star counts. Once the dusty stars are recovered, we classify them as C- or M-type using the criteria outlined in Section 2.4.2.

Paper II adopted the definition set by Blum et al. (2006), who defined the dustiest AGB stars (dubbed extreme AGB or x-AGB stars) in the LMC as those with $J - [3.6] > 3.1$ mag. IR spectroscopy has confirmed that x-AGB stars are dominated by carbon stars, though there are also O-rich examples (Trams et al. 1999; van Loon et al. 2008; Ruffle et al. 2015; Boyer et al. 2015a; Jones et al. 2017). Most of the variable stars detected in the DUSTiNGS survey occupy the same space in $[3.6] - [4.5]$ versus $[3.6] - [4.5]$ as the Magellanic Cloud x-AGB stars, and were classified as such. The *HST* coverage includes 99 of the DUSTiNGS x-AGB variables. Of these, 90 are included in our *HST* catalog and 77 are confidently identified as C- or M-type (Table 4). Seven did not fall within the C or M regions of the *HST* CCD and six are identified as possible contaminants (see Section 2.5).

Visual inspection verifies that nine DUSTiNGS x-AGB variables do not have *HST* counterparts (Table 6). These nine sources have an average IR color of $[3.6] - [4.5] = 1.1$ mag (Figure 7), and include five of the six dustiest sources identified in Paper II; those with slightly bluer *Spitzer* colors in Figure 7 may be somewhat affected by CO absorption in the $4.5 \mu\text{m}$ band. All nine sources are well isolated within $r \gtrsim 3$ pix in the *HST* images, which eliminates crowding as a factor in their non-detection and suggests that they are truly fainter than the sensitivity limit of our *HST* observations. Their *Spitzer* colors closely follow COLIBRI AGB tracks, and we therefore propose that these are AGB stars with very strong circumstellar dust extinction. In fact, their IR colors and absolute magnitudes are similar to the progenitor of the intermediate-luminosity optical transient SN2008S, which may have been an electron-capture SN from a massive AGB star (Prieto et al. 2008; Khan et al. 2010). Alternatively, they could be other red objects such as active galactic nuclei.

By combining the *HST* and *Spitzer* data, we find additional examples of both M- and C-type dusty stars that were not identified as variable x-AGB stars in Paper II, most likely because they were observed at an unfavorable pulsation phase. Altogether, we increase the number of known dusty AGB stars by approximately 50% (Table 4). Most of the x-AGB stars that we identify as AGB stars here are C stars, similar to what is seen in the Magellanic Clouds. However, there are examples of M-type x-AGB stars, most notably in IC 10 (see Section 3.2).

2.4.4. Contamination From K-type Giants

Warmer stellar temperatures in metal-poor systems result in large populations of K-type stars, and it is likely that there is some contamination in both our C- and M-type samples. The super-solar metallicity galaxy M31 shows almost no

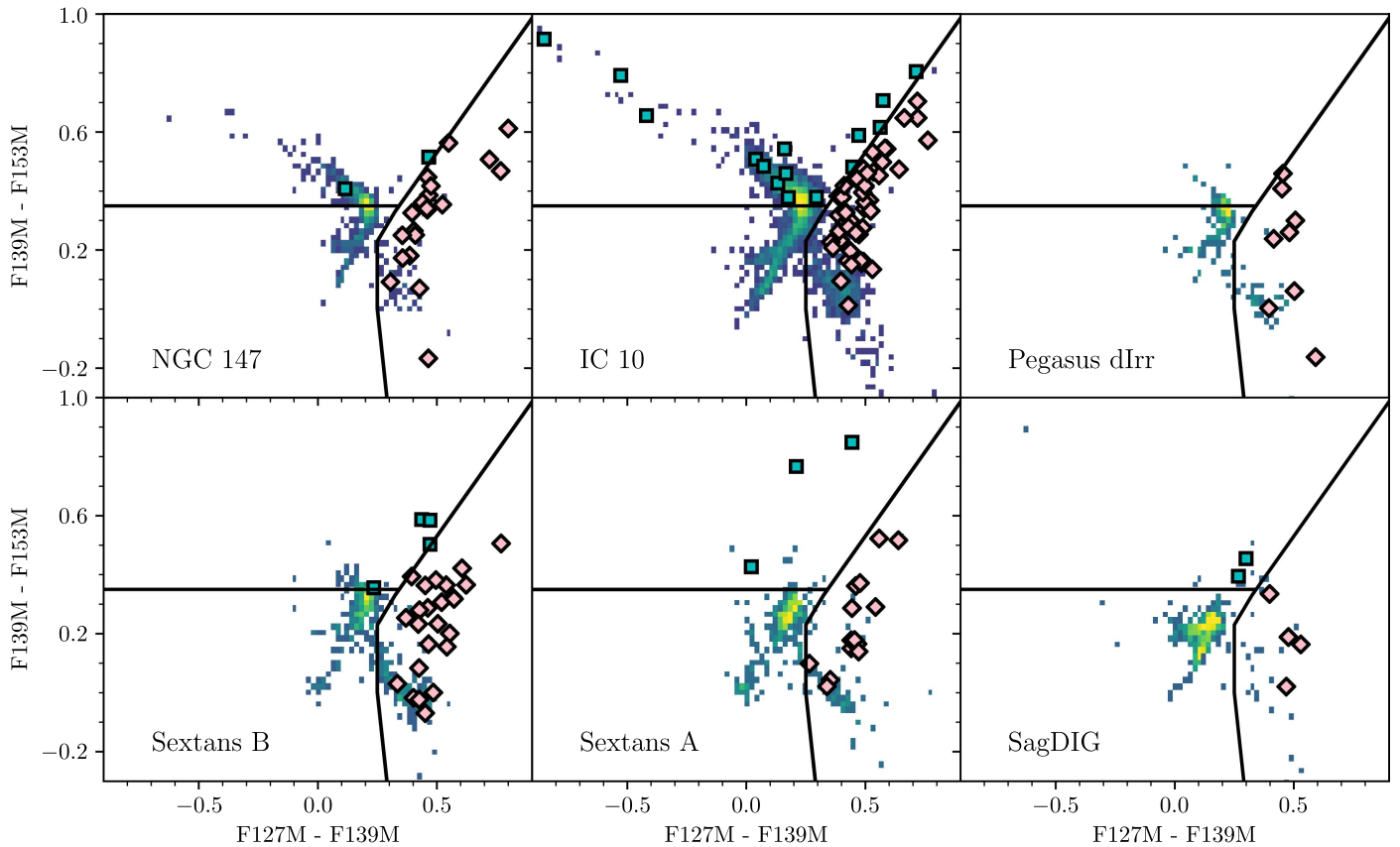


Figure 5. *HST* color–color diagrams. Stars are included if they are brighter than the F153M TRGB. To retain the dustiest examples, stars fainter than this limit are also included if they are brighter than the $3.6\ \mu\text{m}$ TRGB and show $>4\sigma$ excess in the $[3.6]\text{--}[4.5]$ color. Solid lines mark the adopted color cuts chosen to include only stars redder than the “knee” in $F139M\text{--}F153M$ (M 0+). The same cuts are used for all six galaxies. Large cyan squares and pink diamonds mark the dusty M and C stars, respectively, identified by their *Spitzer* colors (see Section 3).

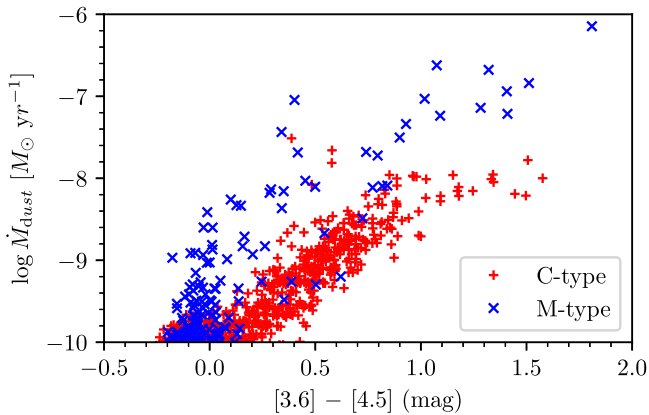


Figure 6. Relationship between dust-production rate and $[3.6]\text{--}[4.5]$ color for SMC AGB stars (Srinivasan et al. 2016). The dust-production rate increases with color for $[3.6]\text{--}[4.5] \gtrsim 0.1$ mag.

contamination from K giants in the same CCD used here (Boyer et al. 2013), while Sextans A and SagDIG show a substantial population of K giants. This is evidenced by the continuous sequence downwards from the knee in the CCD through the entire M/K star model sequence and into the region of the CCD dominated by foreground.

Figure 4 shows a few K-type models within the C star region. We have placed the boundaries of the C star region to minimize this contamination, using the natural breaks in source

Table 6
DUSTiNGS x-AGB Variables without *HST* Counterparts

Galaxy	ID	$[3.6]$ (mag)	$[4.5]$ (mag)	Amp. (mag)
IC 10	115785	17.42 ± 0.06	15.20 ± 0.03	0.62
IC 10	109882	15.61 ± 0.03	14.39 ± 0.03	0.45
IC 10	110204	15.91 ± 0.05	14.58 ± 0.03	0.85
IC 10	111624	15.71 ± 0.07	15.13 ± 0.03	0.74
Sex A	90428	17.01 ± 0.05	15.84 ± 0.05	0.50
Sex A	94477	16.89 ± 0.05	15.45 ± 0.03	0.67
Sex B	85647	15.93 ± 0.02	15.43 ± 0.03	0.21
Sex B	93730	16.38 ± 0.03	15.46 ± 0.03	0.40
Sex B	96433	15.81 ± 0.02	15.10 ± 0.03	0.33

Note. The ID is the DUSTiNGS ID from Papers I and II. The amplitude is the change in $3.6\ \mu\text{m}$ magnitude between the two DUSTiNGS epochs (larger amplitudes are generally indicative of more dust).

density between the M and C star population as a guide (Figure 5).

The M-type sample is highly susceptible to contamination from K-type stars. This is by far the largest source of contamination among the C and M samples, and the strength of the contamination increases in metal-poor galaxies. Even a slight shift in the M/K star division has a strong effect on the ratio of C- to M-type stars, and this is discussed further in Paper V (M. L. Boyer et al. 2017, in preparation).

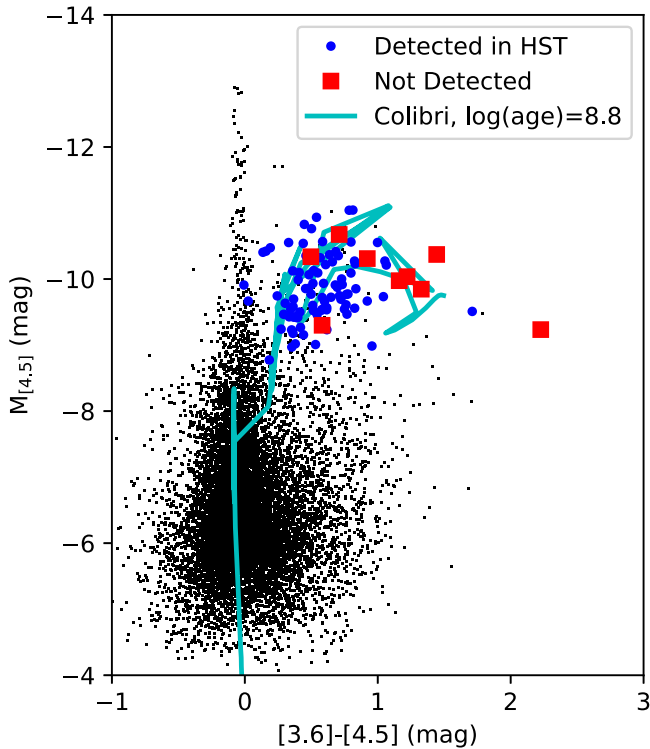


Figure 7. *Spitzer* color–magnitude diagram highlighting the nine DUSTINGS sources not detected in the near-IR with *HST*. Black dots are all of the DUSTINGS sources. Blue points are DUSTINGS x-AGB variables with *HST* counterparts and red squares are those without *HST* counterparts. A COLIBRI isochrone with $\log(\text{age}) = 8.8$ and Nanni et al. (2016) dust growth models ($\log \epsilon_S = -13$) is shown in cyan. The DUSTINGS x-AGB variables (both those with and without *HST* counterparts) generally follow the isochrone.

2.5. Contamination from Other Objects

We do not expect significant contamination from other source types among our sample. Possible contaminants include young stellar objects (YSOs), planetary nebulae (PNe), and post-AGB stars, but the comparatively short lifetimes of these objects make them even more rare than AGB stars.

To minimize contamination, we use data from the SMC as a guide. The Surveying the Agents of Galaxy Evolution (SAGE) program targeted hundreds of sources in both the LMC and the SMC with the InfraRed Spectrograph (IRS) on board *Spitzer* (Kemper et al. 2010) and Ruffle et al. (2015) compared the spectroscopically classified sources to photometric classifications in the SMC. While their near-IR filters are different from ours (they use J and K_S), it is clear from Figure 13 in Ruffle et al. (2015) that dusty AGB stars follow a branch that extends from the TRGB to red colors and faint magnitudes. A similar branch is evident in our near-IR CMDs (Figure 8). YSOs, PNe, and post-AGB stars, on the other hand, tend to be faint and blue in the near-IR. We therefore flag sources to the left of the solid line in Figure 8 as possible contaminants. The slope of the contaminant line was determined using the expected direction of circumstellar extinction from Groenewegen (2012).

Another source of contamination is from red supergiants (RSGs), which have similar infrared properties to AGB stars. RSGs are not easily distinguished with this data set, though they do tend to be warmer than AGB stars, and thus fall toward the lower right end of the M-star sequence in Figure 4. A sample of six confirmed RSGs in IC 10 from Britavskiy et al. (2015) fall below the knee in Figure 4, with some even falling

within the foreground sequence. We expect the number of RSGs in our AGB sample to be small, given their comparative rarity. This is discussed more in Section 3.2.

3. Discussion

3.1. Dusty C Stars

We identify 120 dust-producing carbon stars, almost twice the number detected via two-epoch variability in Paper II. Figure 9 shows the *Spitzer* color–magnitude diagrams for sources detected in the *HST* images. These CMDs are significantly cleaner than those presented by Paper I because the contamination from extended background sources is substantially reduced by including the high-resolution *HST* data. The relative positions of dusty C and M stars in the *Spitzer* CMD are similar, though the dusty C stars tend to be more tightly concentrated than M stars.

Sag DIG and Sextans A are the two most metal-poor galaxies in our sample, with gas-phase ISM metallicities more than an order of magnitude below solar, suggesting that even the youngest stars are very metal-poor. However, both galaxies show a sizeable population of dust-producing C stars, with very similar colors to those seen in more metal-rich galaxies. For C stars, the $[3.6]-[4.5]$ color is approximately proportional to the dust-production rates (Figure 6; Riebel et al. 2012; Sloan et al. 2016; Srinivasan et al. 2016). The similar colors of the C stars across our sample therefore suggest that dust masses are similar at all metallicities. The high efficiency of the third dredge-up at low metallicity (e.g., Karakas et al. 2002) appears to provide metal-poor C stars with plenty of material for dust condensation.

Several dusty sources identified as C stars by the *HST* color definitions from Section 2.4.2 are flagged as possible contaminants based on their positions in Figure 8. This includes some of the reddest sources identified in the survey (see Figure 9). There is a strong possibility that these sources are C-rich PNe or post-AGB stars. In the Magellanic Clouds, the post-AGB stars tend to be brighter and redder than PNe at $4.5 \mu\text{m}$ (Ruffle et al. 2015; Jones et al. 2017). For this reason, we favor the possibility that the contaminants around $M_{[4.5]} \sim -10$ mag are post-AGB stars, including the reddest object in IC 10.

The reddest (non-potential-contaminant) carbon stars in our sample have $[3.6]-[4.5] \sim 1$ mag, which corresponds to a dust-production rate of $\log \dot{M}_{\text{dust}} = -9$ to $-8 [M_{\odot} \text{yr}^{-1}]$, according to the SMC relationship in Figure 6.

3.2. Dusty M Stars

We find a total of 26 dust-producing M-type candidates, comprising 1.2% of the M star population. We list them in Table 7 along with their photometry and classification confidence. The reddest among these have $[3.6]-[4.5] \sim 1$ mag, which corresponds to a dust-production rate of $\log \dot{M}_{\text{dust}} = -7.5$ to $-6.5 [M_{\odot} \text{yr}^{-1}]$ using the SMC relationship in Figure 6.

AGB stars remain O-rich M-type stars both at the low and high ends of the AGB mass range due either to insufficient dredge-up or to HBB, though the exact mass limits depend on the metallicity. Most of the M-type stars we identified in Section 2.4.2 are low-mass AGB stars and are expected to produce only modest amounts of dust (e.g., McDonald et al. 2009, 2011; Boyer et al. 2015a). The significant IR excesses of

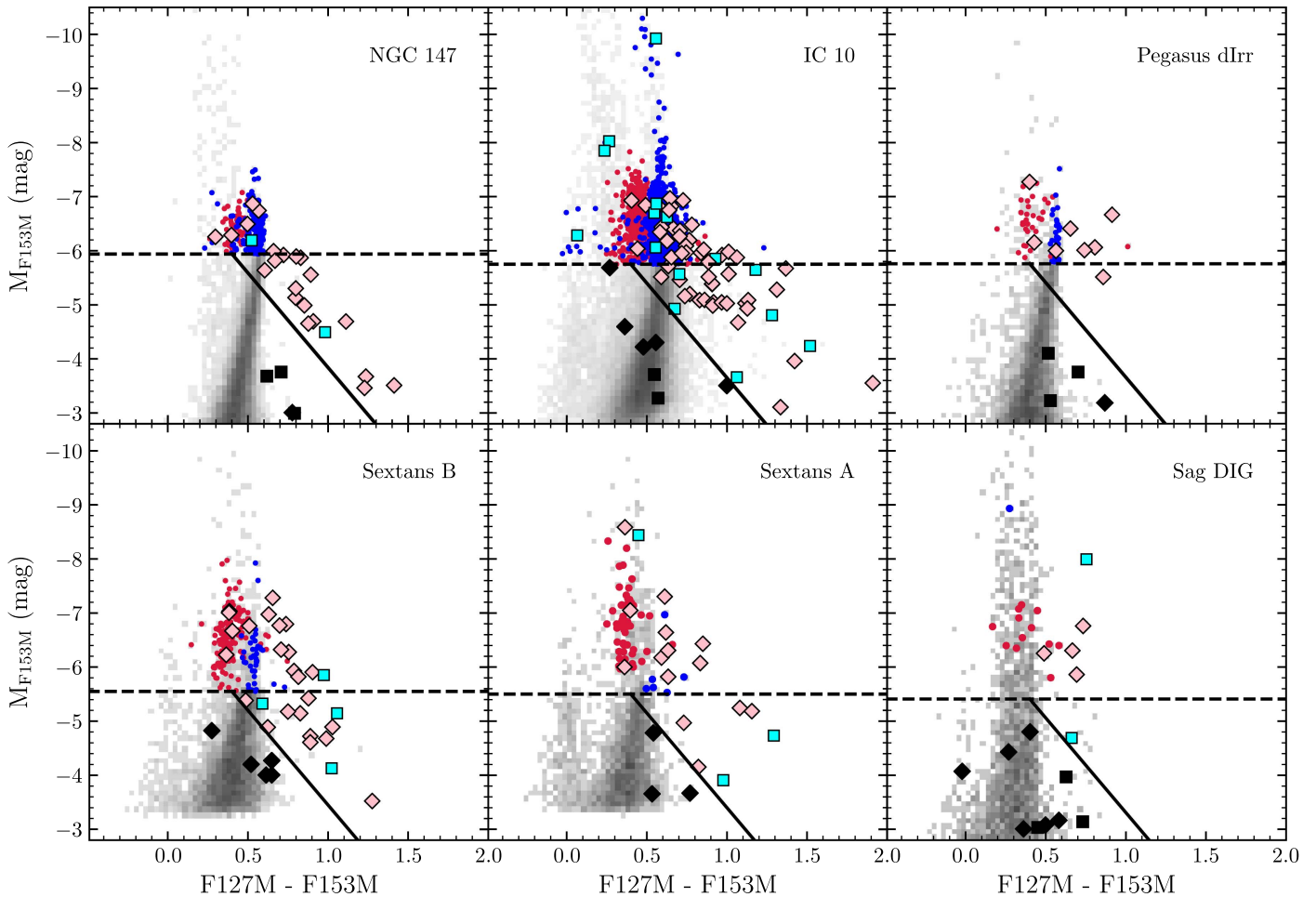


Figure 8. *HST* color–magnitude diagrams with C (red dots) and M (blue dots) stars labeled. Note that late-M-type stars can be very blue in F127M–F153M due to deep water absorption that affects F153M as well as F139M. Large cyan squares are M-type stars with $>4\sigma$ excess in the [3.6]–[4.5] color, indicating the presence of circumstellar dust. Likewise, large pink diamonds are dusty C stars. The dashed line marks the TRGB and the solid line marks the adopted division between likely dusty AGB stars and contaminating sources (see the text). Contaminants (YSOs, PNe, etc.) are marked by solid black squares and diamonds, where the shape indicates whether they were classified as M or C stars, respectively, in the *HST* CCD (Figure 5).

the 26 M-type dusty stars identified here suggests that they are instead HBB AGB stars and are therefore more massive than their C-rich counterparts. Moreover, the dusty M-type stars are mostly confined to within each galaxy’s half-light radius (McConnachie 2012). This suggests they are more massive than the dusty C stars, which are located throughout the spatial coverage of the *HST* data including in fields that are entirely outside the half-light radii (i.e., Fields A in NGC 147 and Sag DIG). Age gradients are expected in dwarf star-forming galaxies (e.g., Aparicio & Tikhonov 2000; Hidalgo et al. 2013, see also Paper III) and this is expected from models of the effects of feedback and stellar migration (e.g., Stinson et al. 2009; El-Badry et al. 2016). Overall, we identify about 1% of the AGB stars as massive M type, similar to the fraction seen in the SMC (Boyer et al. 2011). If confirmed, their high masses and low metallicities make them the closest known analogs to high-redshift dusty AGB stars.

The brightest among the massive AGB candidates may instead be RSG stars, which are expected to destroy all or most of their dust when they explode as supernovae (Lakićević et al. 2015; Temim et al. 2015). It can be difficult to distinguish M-type AGB stars from RSGs—luminosity is often used as a diagnostic, with the classical AGB limit near $M_{\text{bol}} = -7.1$ mag. However, HBB AGB stars have been known to

surpass this luminosity (e.g., García-Hernández et al. 2009). Water absorption is another possible diagnostic; Lancon et al. (2007) notes that water absorption in the near-IR is present in Galactic RSGs with cool effective temperatures ($T_{\text{eff}} < 3100$ K for $\log g = -1$), but is weak compared to the strength of water features in Mira variables. Messineo et al. (2014) use the Rayner et al. (2009) IRTF spectral library to compute a water absorption index and find that the index is large for all Mira-variable AGB stars, and small for semiregular variable AGB stars and RSGs. It follows that the H_2O absorption sequence in the *HST* CCD (Figures 4 and 5) can be used as a diagnostic to separate probable AGB and RSG stars. M-type stars on the water absorption sequence are probable AGB stars, while those at or below the “knee” in Figure 4 may be either less-evolved AGB stars or RSGs. Variability is an additional diagnostic; stars that were identified as variable in DUSTINGS are probable AGB stars, given their large infrared amplitudes.

Based on their H_2O and variability signatures, IC 10 has several candidate dusty M-type AGB stars likely undergoing HBB: 10 identified with high confidence and 5 with low confidence (Table 7). There are two additional high confidence dusty M-type candidates in NGC 147 (#103322) and in Sextans A (#90034). Low-confidence dusty M-type stars either show weak H_2O absorption, fall near the contamination

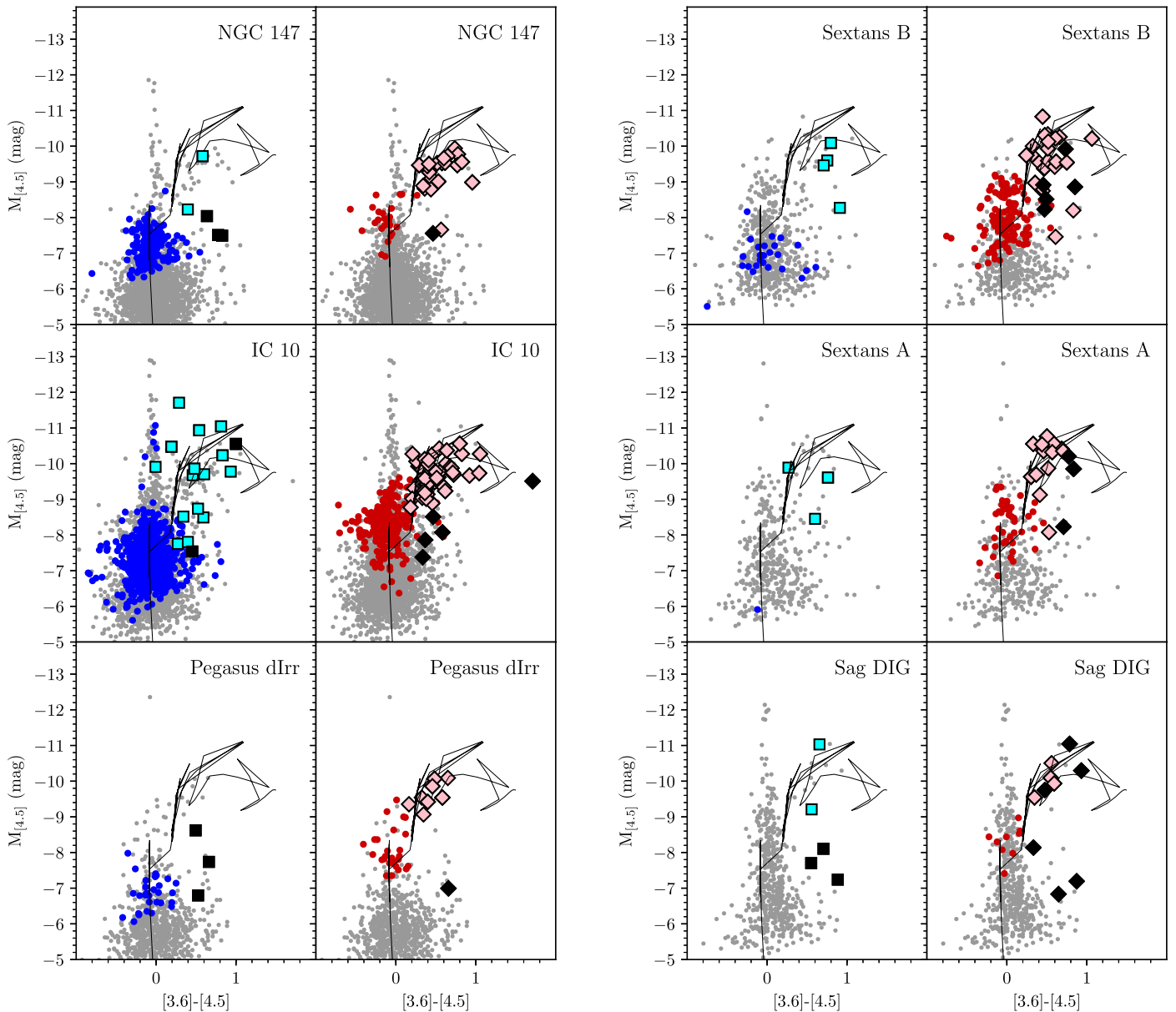


Figure 9. *Spitzer* CMDs with M (blue) and C (red) stars overplotted. Symbols are the same as those in Figure 8. The isochrone (thin black line) is the same one plotted in Figure 7, with $\log(\text{age}) = 8.8$.

cutoff in Figure 8, or fall on the dividing line between C- and M-type stars in Figure 5, and thus a C-rich chemistry cannot be ruled out. Other low-confidence dusty M-type stars are affected by crowding, which may influence the near-IR colors by up to 0.5 mag (as measured by Dolphot; Section 2); these include #91324 and #94328 in Sextans A, #45478 in Sag DIG, and #96092 in IC 10.

The candidates in Sextans A and Sag DIG (especially #44334 and #90034) are of particular interest. The gas-phase ISM metallicities (and thus the metallicities of even the most massive stars) are low for both galaxies ($12 + \log(\text{O}/\text{H}) \lesssim 7.5$), suggesting that stars with primordial abundances can still form a significant dust mass. Whether this occurs via single-star evolution or through a more exotic avenue remains unclear. On the other hand, the high near-IR luminosities of both stars suggests that they may in fact be RSGs, though #90034 in Sextans A does show evidence for water absorption and Star #44334 is a known

long-period variable ($P = 950$ days; Whitelock et al. 2018). Both of these characteristics point to an AGB nature. Three additional confirmed O-rich stars in Sag DIG that were identified by Momany et al. (2014) are included in our near-IR *HST* coverage. These three stars have very red F606W–F814W colors, suggesting substantial circumstellar dust, but we do not detect dust around these stars. Their nature is unclear.

We have too small a sample to draw definitive conclusions, but there is nonetheless no hint of increased dust production at higher metallicities. The dusty M-type stars have remarkably similar properties in the *Spitzer* data, including colors, magnitudes, and pulsation amplitudes. Spectroscopy can definitively classify these sources, especially at wavelengths covering ice features common in YSOs ($3\text{--}15\ \mu\text{m}$) or in the optical, where the Li I 6707 Å and 8126 Å and Rb I 7800 Å lines indicate HBB in AGB stars.

Table 7
Dusty M Stars

Galaxy	DUSTiNGS ID	R.A. Decl.	F127M (mag)	F139M (mag)	F153M (mag)	[3.6] (mag)	[4.5] (mag)	Note
N 147	103322	00 ^h 33 ^m 09 ^s .79 +48 ^d 29 ^m 09 ^s .28	18.849 ± 0.005	18.718 ± 0.006	18.293 ± 0.005	16.59 ± 0.05	16.19 ± 0.06	H
N 147	112780	00 ^h 33 ^m 05 ^s .61 +48 ^d 28 ^m 47 ^s .43	21.006 ± 0.021	20.524 ± 0.018	19.992 ± 0.015	15.28 ± 0.03	14.70 ± 0.03	Lx
IC 10	102032	00 ^h 20 ^m 14 ^s .98 +59 ^d 21 ^m 01 ^s .16	18.883 ± 0.006	18.768 ± 0.006	18.181 ± 0.005	17.10 ± 0.05	16.80 ± 0.05	H
IC 10	105880	00 ^h 20 ^m 12 ^s .38 +59 ^d 19 ^m 41 ^s .95	22.437 ± 0.068	21.889 ± 0.052	21.221 ± 0.037	15.36 ± 0.05	14.88 ± 0.06	L
IC 10	105975	00 ^h 20 ^m 12 ^s .30 +59 ^d 20 ^m 42 ^s .09	15.666 ± 0.001	15.518 ± 0.001	14.955 ± 0.001	13.16 ± 0.03	12.84 ± 0.03	H
IC 10	107349	00 ^h 20 ^m 11 ^s .39 +59 ^d 19 ^m 03 ^s .87	19.530 ± 0.015	19.278 ± 0.017	18.821 ± 0.017	16.68 ± 0.10	16.06 ± 0.07	L
IC 10	112431	00 ^h 20 ^m 07 ^s .99 +59 ^d 19 ^m 31 ^s .74	17.275 ± 0.002	17.727 ± 0.003	16.856 ± 0.002	14.91 ± 0.05 ^a	14.73 ± 0.04	Hx
IC 10	118138	00 ^h 20 ^m 04 ^s .07 +59 ^d 19 ^m 30 ^s .50	17.420 ± 0.003	17.764 ± 0.004	17.029 ± 0.003	14.30 ± 0.03	14.08 ± 0.03	Hx
IC 10	121876	00 ^h 20 ^m 01 ^s .50 +59 ^d 20 ^m 02 ^s .05	18.724 ± 0.005	18.516 ± 0.005	18.010 ± 0.004	15.18 ± 0.03	14.32 ± 0.03	Hx
IC 10	122923	00 ^h 20 ^m 00 ^s .81 +59 ^d 20 ^m 32 ^s .04	18.816 ± 0.005	19.590 ± 0.010	18.596 ± 0.006	16.40 ± 0.03	16.04 ± 0.05	H
IC 10	96092	00 ^h 20 ^m 19 ^s .00 +59 ^d 16 ^m 39 ^s .47	20.783 ± 0.019	20.413 ± 0.020	19.955 ± 0.018	14.35 ± 0.02	13.51 ± 0.03	Lx
IC 10	98013	00 ^h 20 ^m 17 ^s .75 +59 ^d 16 ^m 18 ^s .22	20.568 ± 0.016	19.930 ± 0.012	19.235 ± 0.009	14.18 ± 0.02	13.62 ± 0.03	Lx
IC 10	107616	00 ^h 20 ^m 11 ^s .30 +59 ^d 17 ^m 17 ^s .95	19.040 ± 0.006	18.798 ± 0.006	18.259 ± 0.005	16.36 ± 0.05	15.82 ± 0.06	H
IC 10	108360	00 ^h 20 ^m 10 ^s .81 +59 ^d 16 ^m 12 ^s .22	20.113 ± 0.012	19.591 ± 0.010	19.030 ± 0.008	15.48 ± 0.03	14.85 ± 0.03	L
IC 10	117402	00 ^h 20 ^m 04 ^s .72 +59 ^d 17 ^m 16 ^s .20	20.173 ± 0.012	19.937 ± 0.012	19.315 ± 0.009	17.17 ± 0.07	16.75 ± 0.07	H
IC 10	120247	00 ^h 20 ^m 02 ^s .74 +59 ^d 17 ^m 18 ^s .08	22.315 ± 0.063	21.526 ± 0.042	20.642 ± 0.024	15.74 ± 0.03	14.78 ± 0.03	H
IC 10	120468	00 ^h 20 ^m 02 ^s .58 +59 ^d 16 ^m 52 ^s .46	21.510 ± 0.033	20.860 ± 0.025	20.074 ± 0.017	15.20 ± 0.02	14.69 ± 0.03	Hx
Sex B	84519	10 ^h 00 ^m 03 ^s .61 +05 ^d 18 ^m 55 ^s .29	22.688 ± 0.078	22.249 ± 0.068	21.659 ± 0.053	18.42 ± 0.07	17.50 ± 0.05	L
Sex B	109067	09 ^h 59 ^m 55 ^s .70 +05 ^d 19 ^m 53 ^s .04	20.917 ± 0.020	20.443 ± 0.018	19.937 ± 0.016	16.48 ± 0.03	15.68 ± 0.06	Lx
Sex B	116156	09 ^h 59 ^m 53 ^s .43 +05 ^d 18 ^m 51 ^s .76	21.706 ± 0.059	21.232 ± 0.043	20.644 ± 0.034	16.93 ± 0.05	16.18 ± 0.05	L
Sex B	123385	09 ^h 59 ^m 51 ^s .09 +05 ^d 19 ^m 26 ^s .61	21.060 ± 0.076	20.822 ± 0.073	20.463 ± 0.061	17.02 ± 0.06	16.31 ± 0.05	L
Sex A	90034	10 ^h 10 ^m 59 ^s .54 −04 ^d 40 ^m 58 ^s .69	17.860 ± 0.004	17.835 ± 0.004	17.404 ± 0.003	16.21 ± 0.03	15.94 ± 0.05	H
Sex A	91324	10 ^h 10 ^m 59 ^s .08 −04 ^d 43 ^m 59 ^s .30	22.921 ± 0.098	22.707 ± 0.103	21.936 ± 0.068	17.98 ± 0.05	17.37 ± 0.05	L
Sex A	94328	10 ^h 10 ^m 58 ^s .03 −04 ^d 43 ^m 04 ^s .22	22.413 ± 0.065	21.965 ± 0.057	21.112 ± 0.038	16.98 ± 0.05	16.22 ± 0.05	Lx
Sag	44334	19 ^h 29 ^m 57 ^s .94 −17 ^d 40 ^m 17 ^s .43	18.034 ± 0.004	17.723 ± 0.004	17.256 ± 0.003	14.83 ± 0.03	14.17 ± 0.03	H
Sag	45478	19 ^h 29 ^m 57 ^s .29 −17 ^d 40 ^m 11 ^s .28	21.245 ± 0.050	20.966 ± 0.053	20.559 ± 0.041	16.55 ± 0.06	15.99 ± 0.08	L

Note. Near-IR *HST* and *Spitzer* magnitudes for candidate M-type, dusty AGB stars. Magnitudes are corrected for extinction (see the text). This includes stars in the M-type region of Figure 4 and with $>4\sigma$ excess in [3.6]–[4.5] color. The *Spitzer* magnitudes are from the DUSTiNGS survey (Paper I & II). The “Note” column marks M-type AGB stars identified with high-confidence (H; *HST* colors indicate water absorption) and low-confidence (L; star is near the border of C and M stars, is near the contamination cutoff in Figure 8, or is affected by crowding). An “x” denotes a DUSTiNGS x-AGB variable (those with $>3\sigma$ variability between two *Spitzer* epochs, i.e., a likely AGB star). Non-x-AGB stars may also be variable, but were observed by DUSTiNGS with an unfavorable cadence.
^a The IRAC magnitudes listed for 112431 are from DUSTiNGS epoch 2 because the star is not as red in epoch 1 ($<4\sigma$ excess; Paper I).

3.2.1. Super AGB Stars

Four dusty M-type stars may be examples of super AGB stars: stars just under the mass transition for becoming a high-mass star in which core nucleosynthesis proceeds to iron before a core collapse ($8\text{--}12 M_{\odot}$). Super AGB stars ignite carbon in their cores, leaving behind an ONe white dwarf (Siess 2007), though some super AGB stars may ultimately explode as electron-capture SNe (e.g., Doherty et al. 2015, 2017).

Models from Doherty et al. (2015) suggest that metal-poor super AGB stars can become as much as a magnitude brighter than the classical AGB limit, which is near -9.4 mag in F153M. Star #105975 in IC 10 has $M_{F153M} = -9.9$ mag and is our best super AGB candidate. Of course, there is the possibility this star is a RSG, but its strong water absorption signature (F127M–F139M = 0.07 mag) suggests otherwise.

In addition, star #90034 in Sextans A and stars #112431 and #118138 in IC 10 are within ≈ 1 mag of the classical AGB limit and also show significant water absorption and dust excess. The two IC 10 stars also showed variability in DUSTiNGS. It is thus very likely that these are massive AGB stars, but whether they are super AGB stars remains to be seen.

Additional super-AGB candidates are the nine infrared variables without *HST* counterparts (Table 6). These are among the reddest objects in our sample, and include examples in three galaxies: IC 10, Sextans A, and Sextans B. The *Spitzer* colors and magnitudes are similar to the progenitor of SN2008S (Prieto et al. 2008) and to other intermediate-luminosity IR transients (e.g., Kasliwal et al. 2017).

Detection of Li or Rb in these stars would confirm that they are indeed HBB AGB stars, adding to a very small collection of massive and/or super AGB candidates in the Magellanic Clouds (Plez et al. 1993; Smith et al. 1995; García-Hernández et al. 2009; Groenewegen et al. 2009; Groenewegen & Sloan 2017) and in IC 1613 (Menzies et al. 2015). However, we note that IC 10 is in the direction of the Galactic Plane, so finding a foreground AGB star is conceivable. IC 10 star #105975 is in the *Gaia* Data Release 1 catalog, but has no reported parallax because it is too faint for the Tycho-2 catalog ($G = 20.06$ mag; *Gaia* Collaboration et al. 2016).

3.3. Implications for the Dust Budget

Based on the results in the SMC (see Figure 6; Srinivasan et al. 2016), O-rich AGB stars redder than $[3.6]\text{--}[4.5] \approx 0.1$ mag have dust-production rates that are an order of magnitude or more larger than C-rich stars *with the same color*. In our fields, the dusty C-rich stars outnumber the dusty O-rich sources by factors of about 2–10, but the total dust mass may be more evenly split between silicates and carbon grains if the M-type dust-production rates behave similarly to those in the SMC. The rarity of dust-producing M-type stars makes the balance between O-rich and C-rich dust highly stochastic. Observations with the *James Webb Space Telescope* will provide more reliable estimates of the dust-production rates for entire stellar populations in dwarf galaxies well beyond the Local Group (Boyer 2016).

4. Conclusions












The DUSTiNGS survey identified hundreds of candidate dust-producing AGB stars in nearby galaxies spanning a broad metallicity range, finding that AGB stars can form dust at

metallicities as low as 0.6% solar (Paper II). However, that survey was unable to identify the stars' spectral types, and thus could not infer whether the primary dust species produced is carbon- or oxygen-rich. We surveyed six DUSTiNGS galaxies using medium-band filters on *HST*'s WFC3/IR to identify AGB spectral types. These filters sample the near-IR CN and C_2 features in carbon stars and the H_2O feature in oxygen-rich stars, providing an effective tool for separating C-, M-, and K-type stars. The galaxies surveyed here include 99 candidate dusty stars and span 1 dex in metallicity ($-2.1 < [\text{Fe}/\text{H}] < -1.1$). Altogether, we identify 908 C stars and 2120 M stars among these galaxies; 13.2% and 1.2% of these, respectively, show evidence for dust production (see Table 4). Our conclusions are as follows:

1. Most of the dusty AGB candidates identified in Paper II are confirmed here to be C-type AGB stars, confirming that C-rich AGB stars can form dust in very metal-poor environments.
2. We find 26 dusty M-type stars among our sample, including in our most metal-poor galaxies (Sextans A and Sag DIG). These stars are very likely metal-poor given the low ISM gas-phase metallicities of these galaxies ($12 + \log(\text{O}/\text{H}) = 7.2\text{--}7.5$). Finding dust-producing M-type stars at these metallicities is a surprise; unlike C stars, M-type stars do not to produce their own condensable material so dust production is not expected at low metallicity. Given their dust excess and their central locations within each galaxy, it is likely that these are massive AGB stars. This makes them the closest known analogs to AGB stars at high redshift that may be contributing to galaxy dust budgets as early as 30 Myr after they form.
3. The brightest dusty M-type star in our sample (in IC 10) exceeds the classical AGB limit, but its strong water absorption signature (as evident in the F127M–F139M and F139M–F153M colors) suggests that it is an AGB star rather than a more massive RSG. This star may be an example of a (exceptionally rare) super AGB star ($M_i = 8\text{--}12 M_{\odot}$), which will end its life either as an ONe white dwarf or an electron capture supernova.

Support for *HST* program GO-14073 was provided by NASA through a grant from the Space Telescope Science Institute, which is operated by the Association of Universities for Research in Astronomy, Incorporated, under NASA contract NAS5-26555. Analysis for this work made use of Astropy (Astropy Collaboration et al. 2013). We thank the referee for suggestions that improved the manuscript.

ORCID iDs

- M. L. Boyer  <https://orcid.org/0000-0003-4850-9589>
 K. B. W. McQuinn  <https://orcid.org/0000-0001-5538-2614>
 M. A. T. Groenewegen  <https://orcid.org/0000-0003-2723-6075>
 A. A. Zijlstra  <https://orcid.org/0000-0002-3171-5469>
 J. Th. van Loon  <https://orcid.org/0000-0002-1272-3017>
 G. Sonneborn  <https://orcid.org/0000-0003-1440-9897>
 G. C. Sloan  <https://orcid.org/0000-0003-4520-1044>
 E. D. Skillman  <https://orcid.org/0000-0003-0605-8732>
 O. C. Jones  <https://orcid.org/0000-0003-4870-5547>
 R. D. Gehrz  <https://orcid.org/0000-0003-1319-4089>
 A. Z. Bonanos  <https://orcid.org/0000-0003-2851-1905>

References

- Aparicio, A., & Tikhonov, N. 2000, *AJ*, **119**, 2183
- Aringer, B., Girardi, L., Nowotny, W., Marigo, P., & Bressan, A. 2016, *MNRAS*, **457**, 3611
- Aringer, B., Girardi, L., Nowotny, W., Marigo, P., & Lederer, M. T. 2009, *A&A*, **503**, 913
- Astropy Collaboration, Robitaille, T. P., Tollerud, E. J., et al. 2013, *A&A*, **558**, A33
- Bellazzini, M., Beccari, G., Fraternali, F., et al. 2014, *A&A*, **566**, A44
- Blum, R. D., Mould, J. R., Olsen, K. A., et al. 2006, *AJ*, **132**, 2034
- Boothroyd, A. I., Sackmann, I.-J., & Ahern, S. C. 1993, *ApJ*, **416**, 762
- Boyer, M. L. 2016, *MmSAI*, **87**, 269
- Boyer, M. L., Girardi, L., Marigo, P., et al. 2013, *ApJ*, **774**, 83
- Boyer, M. L., McDonald, I., Loon, J. T., et al. 2008, *AJ*, **135**, 1395
- Boyer, M. L., McDonald, I., Srinivasan, S., et al. 2015a, *ApJ*, **810**, 116
- Boyer, M. L., McDonald, I., van Loon, J. T., et al. 2009, *ApJ*, **705**, 746
- Boyer, M. L., McQuinn, K. B. W., Barmby, P., et al. 2015b, *ApJS*, **216**, 10
- Boyer, M. L., McQuinn, K. B. W., Barmby, P., et al. 2015c, *ApJ*, **800**, 51
- Boyer, M. L., Srinivasan, S., van Loon, J. T., et al. 2011, *AJ*, **142**, 103
- Britavskiy, V., Bonanos, A., & Meher, A. 2015, *IAUGA*, **22**, 2245786
- Conn, A. R., Ibata, R. A., Lewis, G. F., et al. 2012, *ApJ*, **758**, 11
- Dalcanton, J. J., Williams, B. F., Lang, D., et al. 2012b, *ApJS*, **200**, 18
- Dalcanton, J. J., Williams, B. F., Melbourne, J. L., et al. 2012a, *ApJS*, **198**, 6
- Davidge, T. J. 2014, *ApJ*, **791**, 66
- Doherty, C. L., Gil-Pons, P., Siess, L., & Lattanzio, J. C. 2017, PASA, submitted (arXiv:1703.06895)
- Doherty, C. L., Gil-Pons, P., Siess, L., Lattanzio, J. C., & Lau, H. H. B. 2015, *MNRAS*, **446**, 2599
- Dolphin, A. E. 2000, *PASP*, **112**, 1383
- Dwek, E., & Cherchneff, I. 2011, *ApJ*, **727**, 63
- El-Badry, K., Wetzel, A., Geha, M., et al. 2016, *ApJ*, **820**, 131
- Gaia Collaboration, Brown, A. G. A., Vallenari, A., et al. 2016, *A&A*, **595**, A2
- García-Hernández, D. A., Machado, A., Lambert, D. L., et al. 2009, *ApJL*, **705**, L31
- Geha, M., van der Marel, R. P., Guhathakurta, P., et al. 2010, *ApJ*, **711**, 361
- Girardi, L., Groenewegen, M. A. T., Hatziminaoglou, E., & da Costa, L. 2005, *A&A*, **436**, 895
- Goldman, S. R., van Loon, J. T., Zijlstra, A. A., et al. 2017, *MNRAS*, **465**, 403
- Gratton, R., Sneden, C., & Carretta, E. 2004, *ARA&A*, **42**, 385
- Gratton, R. G., Carretta, E., & Bragaglia, A. 2012, *A&ARV*, **20**, 50
- Groenewegen, M. A. T. 2006, *A&A*, **448**, 181
- Groenewegen, M. A. T. 2012, *A&A*, **543**, A36
- Groenewegen, M. A. T., & Sloan, G. C. 2017, *A&A*, submitted (arXiv:1711.07803)
- Groenewegen, M. A. T., Sloan, G. C., Soszyński, I., & Petersen, E. A. 2009, *A&A*, **506**, 1277
- Groenewegen, M. A. T., Wood, P. R., Sloan, G. C., et al. 2007, *MNRAS*, **376**, 313
- Gruendl, R. A., Chu, Y.-H., Seale, J. P., et al. 2008, *ApJL*, **688**, L9
- Hamedani Golshan, R., Javadi, A., van Loon, J. T., Khosroshahi, H., & Saremi, E. 2017, *MNRAS*, **466**, 1764
- Hidalgo, S. L., Monelli, M., Aparicio, A., et al. 2013, *ApJ*, **778**, 103
- Jackson, D. C., Skillman, E. D., Gehrz, R. D., Polomski, E., & Woodward, C. E. 2007a, *ApJ*, **656**, 818
- Jackson, D. C., Skillman, E. D., Gehrz, R. D., Polomski, E., & Woodward, C. E. 2007b, *ApJ*, **667**, 891
- Javadi, A., van Loon, J. T., Khosroshahi, H., & Mirtorabi, M. T. 2013, *MNRAS*, **432**, 2824
- Jones, O. C., Kemper, F., Srinivasan, S., et al. 2014, *MNRAS*, **440**, 631
- Jones, O. C., Woods, P. M., Kemper, F., et al. 2017, *MNRAS*, **470**, 3250
- Karakas, A. I., & Lattanzio, J. C. 2014, *PASA*, **31**, e030
- Karakas, A. I., Lattanzio, J. C., & Pols, O. R. 2002, *PASA*, **19**, 515
- Karakas, A. I., & Lugaro, M. 2016, *ApJ*, **825**, 26
- Kasliwal, M. M., Bally, J., Masci, F., et al. 2017, *ApJ*, **839**, 88
- Kemper, F., Woods, P. M., Antoniou, V., et al. 2010, *PASP*, **122**, 683
- Khan, R., Stanek, K. Z., Prieto, J. L., et al. 2010, *ApJ*, **715**, 1094
- Kimble, R. A., MacKenty, J. W., O'Connell, R. W., & Townsend, J. A. 2008, *Proc. SPIE*, **7010**, 70101E
- Kirby, E. N., Rizzi, L., Held, E. V., et al. 2017, *ApJ*, **834**, 9
- Lagadec, E., Zijlstra, A. A., Sloan, G. C., et al. 2007, *MNRAS*, **376**, 1270
- Lakićević, M., van Loon, J. T., Meixner, M., et al. 2015, *ApJ*, **799**, 50
- Lançon, A., Hauschildt, P. H., Ladjal, D., & Mouhcine, M. 2007, *A&A*, **468**, 205
- Lee, H., Skillman, E. D., Cannon, J. M., et al. 2006, *ApJ*, **647**, 970
- Lorenz, D., Lebzelter, T., Nowotny, W., et al. 2011, *A&A*, **532**, A78
- Makarov, D., Makarova, L., Rizzi, L., et al. 2006, *AJ*, **132**, 2729
- Marigo, P., Girardi, L., Bressan, A., et al. 2017, *ApJ*, **835**, 77
- Mateo, M. L. 1998, *ARA&A*, **36**, 435
- Matsuura, M., Zijlstra, A. A., Bernard-Salas, J., et al. 2007, *MNRAS*, **382**, 1889
- McConnachie, A. W. 2012, *AJ*, **144**, 4
- McConnachie, A. W., Irwin, M. J., Ferguson, A. M. N., et al. 2005, *MNRAS*, **356**, 979
- McDonald, I., Boyer, M. L., van Loon, J. T., et al. 2011, *ApJS*, **193**, 23
- McDonald, I., van Loon, J. T., Decin, L., et al. 2009, *MNRAS*, **394**, 831
- McDonald, I., Zijlstra, A. A., Sloan, G. C., et al. 2014, *MNRAS*, **439**, 2618
- McQuinn, K. B. W., Boyer, M. L., Mitchell, M. B., et al. 2017, *ApJ*, **834**, 78
- McQuinn, K. B. W., Skillman, E. D., Dolphin, A. E., Berg, D., & Kennicutt, R. 2016, *AJ*, **152**, 144
- McQuinn, K. B. W., Woodward, C. E., Willner, S. P., et al. 2007, *ApJ*, **664**, 850
- Méndez, B., Davis, M., Moustakas, J., et al. 2002, *AJ*, **124**, 213
- Menzies, J. W., Feast, M. W., Whitelock, P. A., & Matsunaga, N. 2011, *MNRAS*, **414**, 3492
- Menzies, J. W., Whitelock, P. A., & Feast, M. W. 2015, *MNRAS*, **452**, 910
- Menzies, J. W., Whitelock, P. A., Feast, M. W., & Matsunaga, N. 2010, *MNRAS*, **406**, 86
- Messineo, M., Zhu, Q., Ivanov, V. D., et al. 2014, *A&A*, **571**, A43
- Michałowski, M. J. 2015, *A&A*, **577**, A80
- Momany, Y., Clemens, M., Bedin, L. R., et al. 2014, *A&A*, **572**, A42
- Momany, Y., Held, E. V., Saviane, I., & Rizzi, L. 2002, *A&A*, **384**, 393
- Nanni, A., Marigo, P., Groenewegen, M. A. T., et al. 2016, *MNRAS*, **462**, 1215
- Nowotny, W., Kerschbaum, F., Olofsson, H., & Schwarz, H. E. 2003, *A&A*, **403**, 93
- Plez, B., Smith, V. V., & Lambert, D. L. 1993, *ApJ*, **418**, 812
- Prantzos, N., Charbonnel, C., & Iliadis, C. 2007, *A&A*, **470**, 179
- Prieto, J. L., Kistler, M. D., Thompson, T. A., et al. 2008, *ApJL*, **681**, L9
- Rayner, J. T., Cushing, M. C., & Vacca, W. D. 2009, *ApJS*, **185**, 289
- Ribbel, D., Srinivasan, S., Sargent, B., & Meixner, M. 2012, *ApJ*, **753**, 71
- Rizzi, L., Tully, R. B., Makarov, D., et al. 2007, *ApJ*, **661**, 815
- Rowlands, K., Gomez, H. L., Dunne, L., et al. 2014, *MNRAS*, **441**, 1040
- Ruffle, P. E., Kemper, F., Jones, O. C., et al. 2015, *MNRAS*, **451**, 3504
- Sabbi, E., Anderson, J., Lennon, D. J., et al. 2013, *AJ*, **146**, 53
- Sakai, S., Madore, B. F., & Freedman, W. L. 1996, *ApJ*, **461**, 713
- Saviane, I., Rizzi, L., Held, E. V., Bresolin, F., & Momany, Y. 2002, *A&A*, **390**, 59
- Schlafly, E. F., & Finkbeiner, D. P. 2011, *ApJ*, **737**, 103
- Siess, L. 2007, *A&A*, **476**, 893
- Sloan, G. C., Kraemer, K. E., McDonald, I., et al. 2016, *ApJ*, **826**, 44
- Sloan, G. C., Matsuura, M., Lagadec, E., et al. 2012, *ApJ*, **752**, 140
- Sloan, G. C., Matsuura, M., Zijlstra, A. A., et al. 2009, *Sci*, **323**, 353
- Smith, V. V., Plez, B., Lambert, D. L., & Lubowich, D. A. 1995, *ApJ*, **441**, 735
- Srinivasan, S., Boyer, M. L., Kemper, F., et al. 2016, *MNRAS*, **457**, 2814
- Stetson, P. B. 1987, *PASP*, **99**, 191
- Stinson, G. S., Dalcanton, J. J., Quinn, T., et al. 2009, *MNRAS*, **395**, 1455
- Temim, T., Dwek, E., Tchernyshyov, K., et al. 2015, *ApJ*, **799**, 158
- Tikhonov, N. A., & Galazutdinova, O. A. 2009, *AsI*, **35**, 748
- Trams, N. R., van Loon, J. T., Waters, L. B. F. M., et al. 1999, *A&A*, **346**, 843
- Valiante, R., Schneider, R., Bianchi, S., & Andersen, A. C. 2009, *MNRAS*, **397**, 1661
- van Loon, J. T. 2006, in ASP Conf. Ser. 353, *Stellar Evolution at Low Metallicity: Mass Loss, Explosions, Cosmology*, ed. H. J. G. L. M. Lamers et al. (San Francisco, CA: ASP), 211
- van Loon, J. T., Cohen, M., Oliveira, J. M., et al. 2008, *A&A*, **487**, 1055
- van Loon, J. T., Zijlstra, A. A., Whitelock, P. A., et al. 1998, *A&A*, **329**, 169
- Ventura, P., Criscienzo, M. D., Schneider, R., et al. 2012, *MNRAS*, **424**, 2345
- Weisz, D. R., Dolphin, A. E., Skillman, E. D., et al. 2014, *ApJ*, **789**, 147
- Whitelock, P. A., Menzies, J. W., Feast, M. W., et al. 2009, *MNRAS*, **394**, 795
- Whitelock, P. A., Menzies, J. W., Feast, M. W., & Marigo, P. 2018, *MNRAS*, **473**, 173